Astronomy & Astrophysics

HST far-ultraviolet imaging of DG Tauri

Fluorescent molecular hydrogen emission from the wide opening-angle outflow

P. C. Schneider[1], J. Eislöffel[2], M. Güdel[3], H. M. Günther[4], G. Herczeg[5], J. Robrade[1], and J. H. M. M. Schmitt[1]

[1] Hamburger Sternwarte, Gojenbergsweg 112, 21029 Hamburg, Germany
e-mail: cschneider@hs.uni-hamburg.de
[2] Thüringer Landessternwarte Tautenburg, Sternwarte 5, 07778 Tautenburg, Germany
[3] University of Vienna, Department of Astrophysics, Türkenschanzstrasse 17, 1180 Vienna, Austria
[4] Harvard-Smithsonian Center for Astrophysics, 60 Garden Street, Cambridge, MA 02138, USA
[5] The Kavli Institute for Astronomy and Astrophysics, Peking University, Yi He Yuan Lu 5, Hai Dian Qu, 100871 Beijing, PR China

ABSTRACT

One of the most thoroughly studied jets from all young stellar objects is the jet of DG Tau, which we imaged in the far-ultraviolet with the *Hubble* Space Telescope for the first time. These high spatial resolution images were obtained with long-pass filters and allow us to construct images tracing mainly H_2 and C IV emission. We find that the H_2 emission appears as a limb-brightened cone with additional emission close to the jet axis. The length of the rims is about $0\farcs3$ or 42 AU before their brightness strongly drops, and the opening angle is about $90°$. Comparing our far-ultraviolet data with near-infrared data we find that the fluorescent H_2 emission probably traces the outer, cooler part of the disk wind while an origin of the H_2 emission in the surface layers (atmosphere) of the (flared) disk is unlikely. Furthermore, the spatial shape of the H_2 emission shows little variation over six years which suggests that the outer part of the disk wind is rather stable and probably not associated with the formation of individual knots. The C IV image shows that the emission is concentrated towards the jet axis. We find no indications for additional C IV emission at larger distances, which strengthens the association with the X-ray emission observed to originate within the DG Tau jet.

Key words. stars: individual: DG Tauri – Herbig-Haro objects – ISM: jets and outflows – stars: variables: T Tauri, Herbig Ae/Be – stars: formation

1. Introduction

Stars form by gravitational collapse in molecular clouds. Soon after the initial radial infall ceases, they continue their accretion from a just formed circumstellar disk. This accretion process is accompanied by strong outflow activity. Single classical T Tauri stars (CTTSs) are of particular interest for the study of jets from young stellar objects (YSOs), because their relatively cleared environment allows the jets to be followed almost all the way down to their sources.

The single CTTS DG Tau is the source of one of the first known outflows from a CTTS (HH158, Mundt & Fried 1983), and is still among the brightest optical/near-IR sources so that its properties have been studied by numerous observations (e.g., Mundt et al. 1987; Eislöffel & Mundt 1998; Coffey et al. 2008; Agra-Amboage et al. 2011; Rodríguez et al. 2012). The velocity structure of the DG Tau jet is onion-like with high-velocity parts enclosed by slower material (Bacciotti et al. 2000). There are also indications of jet rotation (Bacciotti et al. 2002; Coffey et al. 2007) in the same sense as the disk (Testi et al. 2002). The jet rotation and onion-like velocity structure are best explained by a disk origin of the outflow (Anderson et al. 2003; Ferreira et al. 2006). Whether there are additional contributions from a stellar wind (e.g., Meliani et al. 2006) or an X-wind launched in the region, where the magnetic fields of the star and the disk interact (Shang et al. 2002), is currently unclear.

Most studies of the DG Tau jet (and YSO jets in general) utilize bright optical and near-IR forbidden emission lines, e.g., [O I] $\lambda6300$, [S II] $\lambda\lambda6716, 6731$, or [Fe II] at $1.64\,\mu$m, which trace plasma temperatures around 10^4 K. These lines originate in the cooling zones of shocks within the jet; for DG Tau shock-velocities of 50 to $100\,km\,s^{-1}$ have been estimated (Lavalley-Fouquet et al. 2000). In addition to the 10^4 K plasma, YSO jets, and the jet of DG Tau in particular, contain plasma of higher *and* lower temperature. Here, we use far-ultraviolet (FUV) observations to trace the low temperature part with molecular hydrogen (H_2) emission of material with only about 2×10^3 K and C IV emission ($T \sim 10^5$) to study the higher temperature regime. Since DG Tau is essentially invisible in the FUV shortwards of about $1600\,$Å, we can follow the H_2 and C IV emission extremely close to the star.

Far-ultraviolet molecular hydrogen emission results from electronic transitions which in general require FUV pumping by Lyα photons, while the ro-vibrational near-IR H_2 lines can be directly stimulated by shocks without FUV pumping (Wolfire & Königl 1991). Fluorescent H_2 in the T Tau system has been studied by Walter et al. (2003) and Saucedo et al. (2003). In this system, the on-source H_2 emission is pumped by broad, self-absorbed Lyα emission which is related to the accretion process. At larger distances from T Tau N, all detected H_2 lines result from fluorescence routes which have pumping transitions close to the rest-velocity of Lyα. Therefore, Walter et al. (2003) concluded that the extended H_2 emission is not pumped by stellar Lyα emission but by emission from local shocks similar to the case in some Herbig-Haro (HH) objects. This interpretation differs from Saucedo et al. (2003) who hypothesize stellar emission

Table 1. Analyzed observations.

Observing date	Instrument	Detector	Filter/Grating	Exposure time	Wavelength range (Å)	Obs. ID.
1981 Oct. 20	IUE	Low dispersion, short wvl.		23.1 ks	1150–1979	SWP15301
1982 Jan. 12	IUE	Low dispersion, short wvl.		26.4 ks	1150–1979	SWP16033
1996 Feb. 08	HST	GHRS	*G160*	16.5 ks	1383–1417	5875
1999 Jan. 14	HST	STIS	*G750M*	16.5 ks	6300–6870	7311
2000 Oct. 22	HST	STIS	*E140M*	2.7 ks	1123–1710	8157
2011 Feb. 17	HST	STIS FUV-MAMA	*G140M*	14.0 ks	1514–1567	12199
2011 Jul. 23	HST	ACS SBC	*F140LP*	1.9 ks	1350–2000	12199
2011 Jul. 23	HST	ACS SBC	*F150LP*	1.9 ks	1450–2000	12199
2011 Jul. 23	HST	ACS SBC	*F165LP*	1.9 ks	1600–2000	12199

as the pumping source while, on the other hand, also requiring shock-heating to achieve the plasma temperature of $T > 1000$ K required for efficient Lyα fluorescence pumping.

Molecular hydrogen has been observed from the region around DG Tau in the FUV (Ardila et al. 2002; Herczeg et al. 2006; Schneider et al. 2013) and in the near-IR (Takami et al. 2004; Beck et al. 2008). The FUV and near-IR H_2 emissions are both concentrated in the forward jet direction. Takami et al. (2004) calculated the momentum flux of the H_2 emitting material for excitation by stellar UV and X-ray photons and found that this momentum flux would be uncomfortably large for a class II source like DG Tau. Therefore, they favor shock heating for the near-IR H_2 lines.

Molecules in YSO outflows can originate from entrainment of ambient molecular, gas-phase formation in a dust-free atomic wind, or from a dusty disk wind (including H_2) with possible H_2 reformation. The spatial structure of the H_2 emission will constrain its origin as one expects the molecular part of a dusty disk wind located outside the atomic region while, for example, H_2 reformed behind shocks would be preferentially located in the path of the optical jet. Several authors found that blueshifted fluorescent H_2 emission is probably associated with outflows (Ardila et al. 2002; Herczeg et al. 2006; France et al. 2012). A prime example for this interpretation is RW Aur due to the large velocity-shift of the H_2 emission.

The high-temperature part of jets ($T \gtrsim 10^6$ K) can be traced by X-ray emission. The jet of DG Tau was the first CTTS jet discovered in X-rays (Güdel et al. 2005, 2007). The favorable viewing geometry with a jet inclination close to 45° allowed Schneider & Schmitt (2008) to separate the hard coronal X-ray component from a softer X-ray component suspected to originate in the jet. The mean distance of the soft X-ray photons from DG Tau stays constant within six years (Güdel et al. 2012) and thus contrasts the optical forbidden emission lines (FELs), where proper-motion is clearly present (Eislöffel & Mundt 1998; Dougados et al. 2000). The intermediate temperature region has been studied with *Hubble* Space Telescope (HST) Space Telescope Imaging Spectrograph (STIS) long-slit data of FUV C IV emission (peak formation temperature 10^5 K), showing that the $\sim 10^5$ K plasma is almost co-spatial with the stationary X-ray emission where the H_2 emission has a minimum (Schneider et al. 2013). This FUV spectrum is, however, limited to the region close to the jet axis owing to the slit-width of 0.″2, and the images presented here cover a much larger region around DG Tau (Field of view (FOV): 32 × 32 arcsec).

Our paper is structured as follows. We describe the observations and the data reduction including a description of the H_2 and C IV image construction in Sect. 2. Results and discussion of H_2 (Sects. 3 and 4), C IV emission (Sect. 5), and the outer knots

(Sect. 6) are divided into individual sections. We close with a summary and conclusions in Sect. 7.

## 2. Observations and data reduction

2.1. Observations

In addition to our new HST FUV images we use a number of archival FUV observations of DG Tau. Specifically, we use International Ultraviolet Explorer (IUE) spectra to constrain the broadband FUV spectrum (observation dates 1981 and 1982), high resolution FUV spectra obtained with the Goddard High Resolution Spectrograph (GHRS) onboard HST covering about 1.″74 around DG Tau (observation date 1996), high resolution FUV Echelle spectra obtained with HST STIS covering the inner region around DG Tau (0.″1 × 0.″2, observation date 2000), and FUV long-slit spectra covering the region around the jet axis (observation date 2011). For the morphological comparison of our FUV images with the low temperature plasma seen in bright forbidden emission lines, we use the reconstructed image obtained from seven consecutive long-slit optical HST spectra obtained in 1999.

Our new DG Tau FUV images were taken with the Advanced Camera for Surveys (ACS) using the Solar Blind Channel (SBC). We obtained images in three long band-pass filters (*F140LP*, *F150LP*, and *F165LP*) within two consecutive HST orbits (see Table 1). Two separate images were obtained in each filter and co-added for analysis. To minimize the relative offsets between the two images obtained with the same filter, they are registered using `tweakshifts` from the PyRAF `multidrizzle`-package prior to co-adding them. The relative offsets for the exposures taken within the same orbit are negligible ($\lesssim 0.1$ pixel); only the two *F150LP* images separated by an earth occultation have a relative offset of 0.4 pixel (12 mas).

Figure 1 shows the three FUV images. The position angle (PA) of the jet is about 225°, which is not ideal for displaying purposes, so all images were rotated by 45°, i.e., the forward jet now faces towards the right. We clearly detect emission from the immediate region around DG Tau and from two outer knots at about 7″ and 14″. The background estimated from source-free circular regions with $r = 2.″5$ is small compared to the emission. The signal to background is >4 (20) within the innermost 1.″2 (0.″5). Background subtraction was performed using the mean obtained from three $r = 2.″5$ circles. Spatial fluctuations of the background are less than 20%.

The longpass filters have overlapping throughputs longwards of their cut-off wavelengths, i.e., the *F140LP* image includes all the emission seen in the *F150LP*. The throughputs[1] are shown in Fig. 2 overplotted onto the archival IUE spectra of DG Tau.

---

[1] `http://www.stsci.edu/hst/acs/analysis/throughputs`
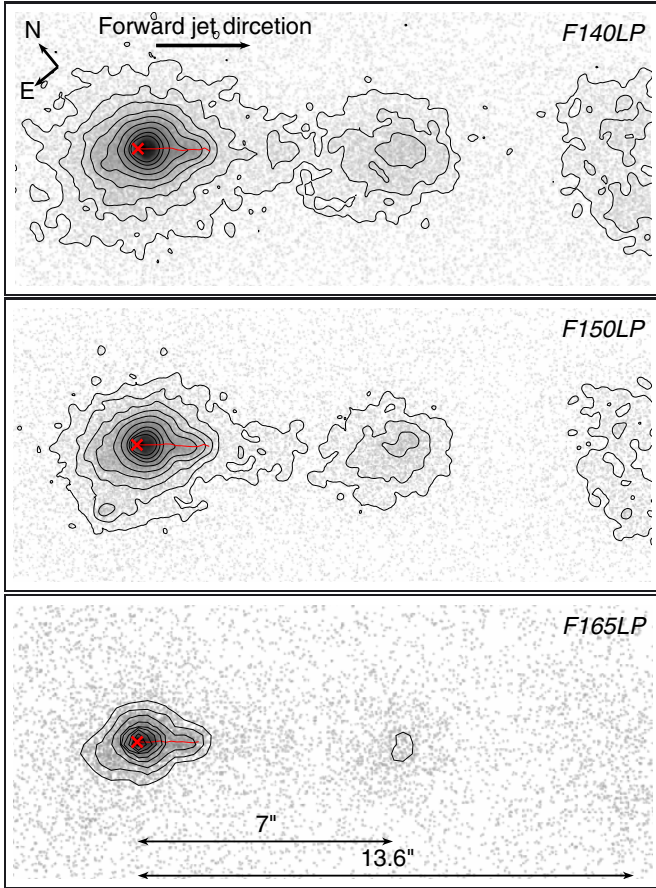
Fig. 1. FUV images of the DG Tau jet. *From top to bottom*: *F140LP*, *F150LP*, *F165LP*. The ranges of the logarithmic scaling differ between panels. Contour levels are equal in all frames, they start at 2 counts/pix (smoothed by a Gaussian of 0.″25) and increase in steps of a factor of two. The cross indicates the position of DG Tau (the size of the cross gives the uncertainty).The outermost emission knot is at the edge of the detector, and its bow/apex is outside the field of view. The red line indicates the jet center.

Additionally, photons with wavelength around 3000 Å increase the count rate due to the red leak of the ACS SBC. We constructed a broadband spectrum using IUE data complemented by STIS G430L data scaled to smoothly match the IUE spectrum and find that up to 17% of the counts in the *F165LP* images might result from photons with $\lambda > 1900$ Å (lower fractions pertain to the other filters). However, those photons are effectively removed during the following procedures.

2.2. The FUV spectrum of DG Tau

Our aim is to extract images in H_2 and C IV from three long-pass filter images (*F140LP*, *F150LP*, and *F165LP*[2]) using difference images. Therefore, we have to analyze the spectral origin of the detected photons. Since their wavelengths are between about 1350 and 2000 Å, only two archival IUE spectra cover the whole bandpass (we omit the short exposure from 1981 Jul. 30, see Table 1 for observational details). These spectra (shown in Fig. 2) were obtained in 1981 and 1982. They have a FOV of about $10'' \times 20''$ so that they contain emission from DG Tau as well as from its jet. The two IUE spectra differ slightly in

---

[2]   The filter names indicate their short wavelength cutoff in nm.

Table 2. Contribution of strong atomic lines to the observed counts in the difference images estimated from the IUE spectra.

Line	Wavelength (Å)	Flux 10^{-15} erg s^{-1}	Count fraction in difference image	
Si IV[a]	1388−1409	38 (≲4.5)	*F140−F150*:	30% (4%)
C IV	1542−1557	55 (20)	*F150−F165*:	18% (9%)
He II	1634−1646	29	*F150−F165*:	5% (6%)
[O III]	1657−1669	36	*F150−F165*:	3% (3%)

Notes. Values in brackets are derived from the STIS E140H or GHRS spectra. The filters are abbreviated as F plus cutoff wavelength. [a] Includes emission from [O IV].

some wavelength regions, but most features are visible in both exposures.

In the wavelength range relevant for our HST FUV images, the spectra of CTTS contain atomic emission lines like C IV, molecular hydrogen emission lines, and a weak continuum (sometimes with additional emission from ro-vibrational bands of CO, e.g., Schindhelm et al. 2012). Our HST G140M spectrum of DG Tau and its jet around the C IV doublet ($\lambda = 1514−1567$ Å, Schneider et al. 2013) does not show any hint of continuum or CO emission. Therefore, the part of the DG Tau FUV spectrum relevant for our images is dominated by atomic and H_2 emission lines without any significant continuum contribution.

For the atomic emission, only a few lines can rival the strong C IV doublet at about 1550 Å and might contribute significantly to our images (essentially lines from Si IV, He II, [O III], and O IV]). An estimate of their contributions can be obtained from the two IUE spectra by integrating the flux within ±6 Å around the nominal position of these lines (this region includes about 95% of the line flux for a line shift below 300 km s^{-1}). Since these regions also include strong H_2 lines, we use an archival HST GHRS spectrum (see Table 1 and Ardila et al. 2002) to further constrain the emission from Si IV and O IV] lines around 1400 Å. This spectrum covers a sufficiently large region around DG Tau to include jet emission (FOV: 1.″74 × 1.″74). It demonstrates that Si IV and O IV] emission are at most marginally present since all emission lines consistently match with H_2 lines (see also Ardila et al. 2002). We derive an upper limit of ≲4.5 × 10^{-15} erg s^{-1} from fitting a set of Gaussians to the emission lines in the GHRS spectrum. No high spectral resolution data of the He II and [O III] lines covering DG Tau *and* the jet exist so that we cannot improve the estimate based on the IUE spectrum for these lines. Their contributions are given in Table 2. The total luminosity excluding the wavelength regions of strong atomic emission lines is about 3.5×10^{-13} erg s^{-1} (1300−1650 Å) and is almost exclusively caused by H_2 emission.

The observed count-ratios of 1:0.67:0.16 (*F140LP*:*F150LP*: *F165LP*) are close to the expectation from the IUE spectra (1:0.71:0.21) using the counts within a circle of 0.″3 around the brightest part of the emission. The observed count-rates are slightly higher than expected from the IUE spectrum; the largest discrepancies (a factor of about 1.3) pertain to the *F140LP* filter, which might be due to cross-calibration issues and/or minor source-variability. These two facts suggest that today's overall spectrum is comparable to the IUE data, which means that we can use the estimates obtained from the IUE and GHRS spectra to identify the dominating contributions to the filter images.
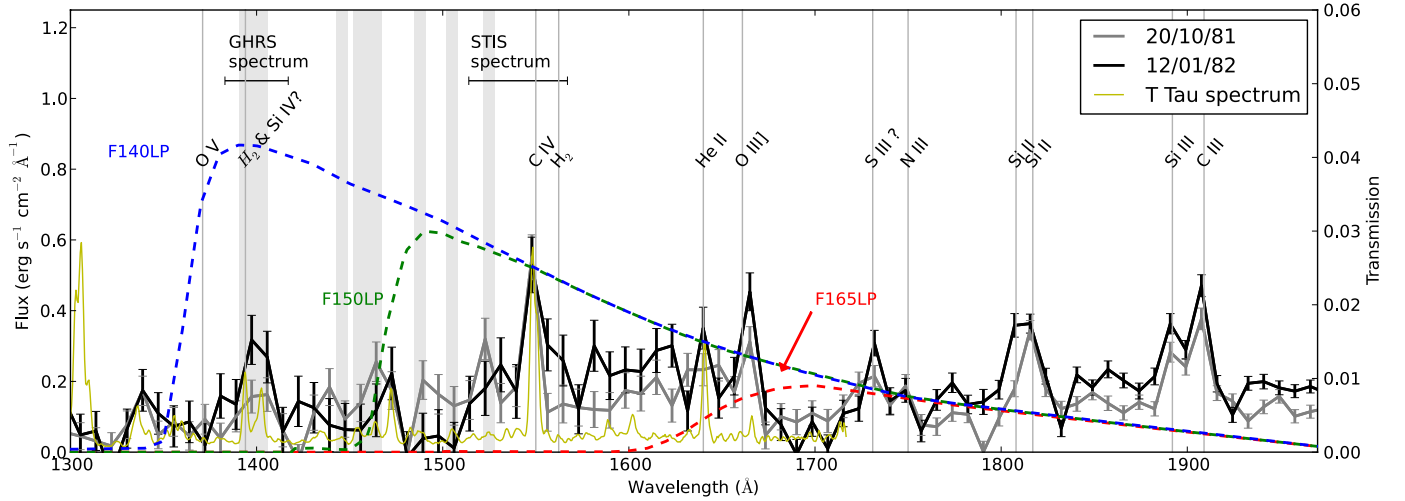
Fig. 2. Re-binned IUE FUV spectra of DG Tau with filter transmission curves of the ACS images superimposed (right axis). Strong lines are labeled and the band-passes of the high-resolution spectra are indicated. The filter efficiencies are indicated by the dashed lines (right axis). For comparison, the higher resolution HST STIS spectrum of T Tau is also shown (yellow). The gray-shaded regions indicate strong H_2 lines.

2.3. Spectral contributions to the filter images

Using specific combinations of the filter images, we can construct images tracing mainly H_2 and C IV emission. Convolving the IUE spectra with the detector response, we find that strong atomic emission lines contribute $\lesssim 4\%$ to the $F140LP-F150LP$ difference image. Furthermore, an H_2 model based on branching ratios and the strongest H_2 lines detected in the E140M spectrum already reproduces $\gtrsim 80\%$ of the flux below 1500 Å. Therefore, the $F140LP–F150LP$ image is largely dominated by H_2 emission and we estimate that atomic emission lines contribute only marginally to the recorded signal.

Within the $F150LP-F165LP$ difference image, strong atomic lines contribute $\lesssim 26\%$ of the observed counts. Most of the atomic emission in this spectral region is C IV emission (about 18%) with some additional contribution from He II and [O III] ($\lesssim 8\%$ of the counts). Thus the $F150LP-F165LP$ difference image is, like the $F140LP – F150LP$ image, again dominated by H_2 emission as spectra around 1550 Å show no continuum emission. To extract the C IV emission (representative of any non-H_2 emission), the H_2 emission, which contributes most of the counts, must be removed. Convolving the IUE spectra with the ACS/SBC filter responses and summing the wavelength-regions without the strong atomic lines mentioned above, we find that $F140LP-F150LP$ image contains 70% of the H_2 counts of the $F150LP-F165LP$ image[3]. A similar value is obtained from the HST STIS E140H spectrum (Herczeg et al. 2006), excluding the same wavelength regions although this spectrum covers only the innermost 0.′′1 of the jet, i.e., only a fraction of the H_2 emission. These values differ from an H_2 model based on branching ratios using the H_2 lines measured in the E140H spectrum. Within the $F150LP-F140LP$ wavelength range, the predicted total flux of this branching ratio model approximately matches the observed total flux, but falls short of the measured flux longwards of about 1500 Å, i.e., it misses lines. Therefore, we prefer the results obtained by convolving the observed flux with the detector responses.

Assuming that the spatial distribution of the H_2 emission traced by the $F140LP-F150LP$ and $F150LP-F165LP$ images is similar, subtracting the H_2 image (i.e., $F140LP-F150LP$) scaled as indicated above from the $F150LP-F165LP$ image should eliminate the H_2 emission of the $F150LP-F165LP$ image so that only atomic (mainly C IV) emission should remain. Given that our STIS long-slit spectrum does not indicate an evolution of the H_2 lines with position along the jet and that one fluorescence route often contributes to both images, the error induced by a different spatial morphology of the H_2 emission above and below about 1500 Å is likely to be negligible. This scaling, however, produces negative residuals[4] which we attribute to an overestimation of the H_2 counts. To avoid strong negative residuals, we use a scaling of 1.2, which reduces the negative residuals while preserving an impression of the problematic region. The count-rate of the C IV image is 1.7 ± 0.25 times higher than expected based on the C IV luminosity in our STIS G140M spectrum (the error corresponds to a 10% change of the H_2 scaling). We note that this image probably includes a small ($\lesssim 30\%$) contribution from other atomic lines. The remaining discrepancy might be due to time variability or cross-calibration problems.

2.4. Alignment of the images

The location of the image on the detector depends on which filter is chosen, because the detector and the filters are tilted with respect to the chief ray. Therefore, we took special care aligning the individual filter images as described in the following.

We applied the known filter shifts given in the instrument handbook (Sect. 5.5.3, Hernandez et al. 2012) to the $F140LP$, $F150LP$, and $F165LP$ images. These shifts are accurate to within about one pixel (30 mas). There are no point sources that can be used as references in the field of view and DG Tau itself is invisible shortwards of ~1600 Å where most of the counts in the $F140LP$ and $F150LP$ images originate. Therefore, the alignment of the images cannot be improved without additional assumptions.

For the alignment perpendicular to the jet axis we assumed that the emission close to DG Tau is symmetric around the jet

---

[3] From our recent STIS long-slit spectrum we know that about 85% of the flux within 1542−1557 Å is actually C IV emission and we corrected the fraction accordingly.

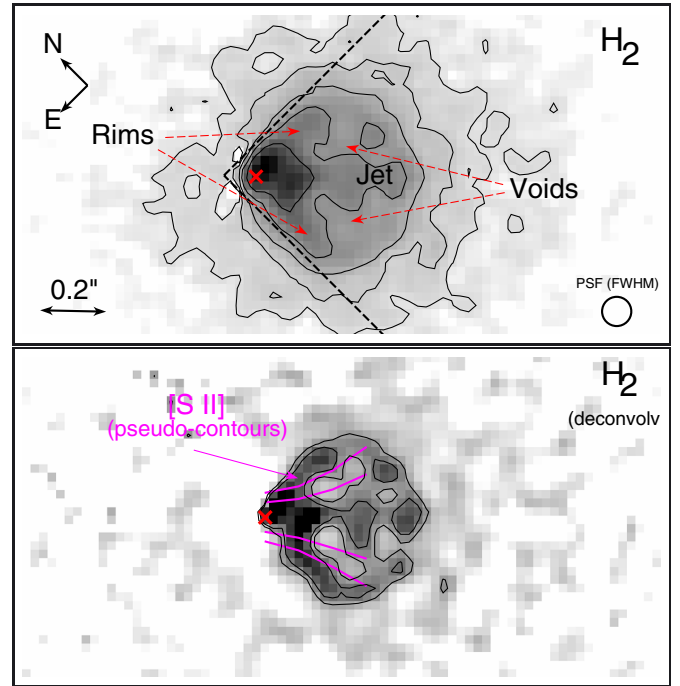[4] This finding is unrelated to the subtraction of the $F165LP$ image.

axis so that the emission centroid perpendicular to the jet axis should match in all filters. By fitting Voigt profiles to the region within 125 mas around the brightest part of the emission we aligned the centroids with shifts up to about 0.5 pixel (15 mas).

The alignment along the jet axis was done assuming that photons with relatively long wavelengths dominate the emission close to DG Tau and we match the images on the side of DG Tau, while allowing them to differ in the forward jet direction (effects caused by the Point Spread Function (PSF) are only a few percentage points and thus negligible). The required shifts are 0.25 and 0.5 pixel (7.5 and 15 mas), respectively.

We checked these shifts by comparing the spatial count distribution in the $F150LP-F165LP$ image with our STIS G140M spectrum obtained five months before the ACS images. This STIS G140M observation covers only the wavelength range from 1514 Å to 1567 Å, while most of the detected photons originate from a much larger wavelength range (approximately from 1500 to 1650 Å). However, the emission is dominated by H_2 emission in the $F140LP$ and $F150LP$ images (see Sect. 2.2). Therefore, we scaled the H_2 emission seen with the G140M as suggested by the IUE spectrum (see Sect. 2.2) and compared the projections from the long-slit spectrum (H_2 and C IV emission) and from the images along the jet axis. These projections agree very well and we estimate an error of $0\rlap{.}''05$ for the spatial zero-point. Similarly shifting the $F165LP$ and $F150LP$ images against each other results in a reduced agreement between the projection and the long-slit data. A proper-motion velocity of $300\,\mathrm{km\,s^{-1}}$, which is typical for optical knots in the DG Tau jet, would result in an observed shift of $0\rlap{.}''13$ between the STIS spectrum and the ACS images. However, the dominating H_2 emission is about three to four times slower (Schneider et al. 2013) so that a maximum offset of about $0\rlap{.}''03-0\rlap{.}''04$ is expected, i.e., comparable with the registration accuracy. After this procedure the peak in the $F165LP$ is 6 mas (0.2 pixel) downstream of the estimated DG Tau position.

2.5. Construction of the H_2 and C IV images

Direct subtraction of the $F150LP$ from the $F140LP$ image results in unphysical negative residuals close to DG Tau which cannot be avoided by changes of the image registration. Inspection of the spatial extent of the emission perpendicular to the jet axis shows that the emission in the $F140LP$ filter is more extended than in the $F150LP$ filter; the FHWM perpendicular to the jet axis is approximately 29% larger. According to synthetic Tiny Tim[5] models, differences between the two filters are only 2%. While the difference in the spatial extent might be partly physical, the negative residuals clearly demonstrate that there are additional instrumental artefacts. We checked that neither thermal settling (the second $F140LP$ image shows a larger FWHM than the first $F140LP$ image) nor spacecraft pointing anomalies (the jitter-files show no anomalies) can explain this property. Inspection of calibration images shows that the spatial sizes of point-sources agree reasonably with the Tiny Tim expectation; however, some show differences between the two filters almost as large as those found for the spatial extent perpendicular to the jet axis in our images. Therefore, we had to smooth the $F150LP$ and $F165LP$[6] images with a Gaussian of 32.5 mas to facilitate the construction of the difference images. We checked that this

---

[5] http://www.stsci.edu/hst/observatory/focus/TinyTim
[6] The $F165LP$ needs to be smoothed as well to allow a comparison with results obtained from the $F140LP$ image.

Fig. 3. *Top*: Inner part of the H_2 emission. Contours start at 10 counts per pixel increasing by a factor of two. The dashed lines indicate the cone used to extract the radial dependence of the count rate. *Bottom*: Deconvolved H_2 image. The magenta lines indicate the region containing 68% and 90% (outer lines) of the [S II] emission in the velocity range +25 to –120 km s^{-1} perpendicular to the jet axis.

procedure does not significantly change the spatial shape of the emission in the difference images.

2.6. Deconvolution of the H_2 image

The H_2 image shows spatial structure on the same scale as the PSF. To improve this image, we created an artificial PSF for the H_2 image using the mean Tiny Tim PSF of the $F140LP$ and $F150LP$ images smoothed by the same Gaussian as the $F150LP$ data for the difference image. We do not deconvolve the individual images, because those deconvolved images already include different artefacts at similar iteration levels which would be transfered into the difference images. We think that deconvolving the difference image provides a better solution in our case. We note that the Tiny Tim PSFs for the $F140LP$ and $F150LP$ images differ only slightly for the spectrum at hand. We used the Richardson-Lucy deconvolution with 50 iterations implemented by arestore in the CIAO tools[7] (Fruscione et al. 2006).

3. Molecular hydrogen: results

The H_2 images obtained by the procedures described above are shown in Fig. 3.

3.1. Spatial structure

The H_2 emission consists of a pronounced bright rim, emission along the central jet axis distinct from the rim, and bright emission close to DG Tau. The spatial morphology resembles an outflow-cavity wall structure; however, we argue in Sect. 3.4

---

[7] see http://cxc.harvard.edu/ciao/intro/tools.html

that the void in H_2 emission is probably filled with other outflowing material so it is not a cavity. Consequently, we speak of the rims when dealing with the V-shaped feature. On the other hand, it is possible that the DG Tau jet will develop into a jet-cavity wall structure at larger distances from DG Tau. Since we do not have data on this region, we will focus on the inner part of the jet/outflow.

We find an opening angle of about 90° between the two rims. Following the rim towards the DG Tau position, both edges intersect very close to the expected DG Tau position. From visual inspection, we find that the rims would intersect a flat disk within a few AU from DG Tau. The rim has a length of approximately 0.″3 (projected 42 AU). Comparing the projection perpendicular to the rim in the $F140LP$, which is dominated by H_2 emission with a Tiny Tim model of a linear feature, we find that the spatial distribution of the emission close to DG Tau resembles the PSF more closely than it does farther away. This indicates that the (projected) sharpness of the rim decreases with increasing distance to DG Tau. Overall, the emission decreases beyond a radial distance of approximately 0.″45. The outer (downstream) edge and the large structure appear almost circular. A circle of radius 0.″25 encloses more than two thirds of the emission.

3.2. Outflow direction

To determine the jet center as a function of distance to the source, we fit Gaussians to slices extending 0.″15 along the jet axis. Since the difference images might contain artificial effects due to registration errors, we use the $F140LP$, $F150LP$, and $F165LP$ images directly. The fits were performed using the emission within 0.″5 from the iteratively determined jet axis and the results are shown in Fig. 1. Within the inner 2″ the signal is sufficient for this procedure and a straight jet gives a PA of 224.6 ± 0.2° ($\chi_{red} \approx 1.0$) compatible with previous estimates (e.g., 226°; Solf & Boehm 1993).

There is also some asymmetry within the jet; for example, extracting the counts between 0.″1 and 0.″3 at both sides of the jet center, we find the northwestern side slightly brighter than the southeastern at the 10% level. Although these asymmetries are small, they show that inhomogeneities within the outflow are already generated close to the source before interactions with the ambient medium take place. Furthermore, the locations of the jet centers show an additional substructure which looks like wiggling (cf. red line in Fig. 1). Although the statistical error on each data point is approximately similar to its distance to the straight axis, the offsets are consistent between the filters and so are probably not purely statistical. The half opening angle of the potential wiggling amplitude is below two degrees. Given the substructure of the outflow, the small variations of the jet center probably result from the slight asymmetries in the emission rather than from a change in the outflow direction.

3.3. Comparison with near-IR H_2 data of DG Tau

Indications for the V-shaped H_2 feature are also seen in near-IR integral field data of DG Tau obtained with Keck (observation date 2005 Oct 26, Beck et al. 2008). These authors observed a variety of near-IR H_2 lines and in particular present an image of the outflow in the $v = 1-0 S(1)$ line at 2.12 μm. A similar spatial distribution was probably also present in the Subaru data of Takami et al. (2004), since convolving the emission within the inner 0.″5 of the forward jet with a Gaussian approximating their seeing conditions results in a Gaussian FWHM of 0.″5, which is

quite similar to the reported 0.″6. Thus, the H_2 emission appears stationary over almost one decade. A similar V-shaped structure of near-IR H_2 emission has also been reported for HL Tau by Takami et al. (2007).

3.4. Relation to the optical jet

We compare the H_2 with low-temperature plasma ($T \sim 10^4$ K) as traced by [S II] $\lambda6731$ emission in Fig. 3 (bottom). The low-velocity part of the [S II] emission appears to be located close to DG Tau at all times, i.e., within the innermost 0.″2 or so (Lavalley et al. 1997; Schneider et al. 2013). To check the spatial relation of both components we compare the distribution of the H_2 emission with an artificial image of the low-velocity [S II] emission (integrated between +25 and −120 km s^{-1}) obtained by combining seven consecutive HST long-slit spectra. This [S II] image covers the innermost ±≈0.″25 perpendicular to the jet axis. Its spatial resolution is about 0.″1. Details of the data processing are provided by Bacciotti et al. (2000, 2002) and Maurri et al. (2013). Since this optical image has a lower spatial resolution than the FUV data, we fit Gaussians to the [S II] emission perpendicular to the jet axis to estimate the spatial extent. Figure 3 shows the 1-σ width of the Gaussians corrected for our estimate of the instrumental PSF width[8], i.e., the region containing 68% of the [S II] emission. We find that the H_2 emission extends to larger jet radii than the [S II] emission (see Fig. 3, bottom), i.e., the [S II] emission is located between the H_2 rims. The initial opening angle of the [S II] emission is also smaller than that of the H_2 emission. However, beyond about 0.″4 from DG Tau the [S II] emission extends to larger jet radii than the FUV H_2 emission. This might be related to the bubble-like feature seen in the [S II] data.

4. Molecular hydrogen: discussion and interpretation

Most of the observed FUV H_2 emission lines are fluorescently excited by Lyα photons[9] which requires H_2 temperatures around 2000 K. Therefore, the FUV H_2 emission traces the amount of warm H_2 *and* the local Lyα radiation field. In CTTS, the H_2 emitting gas can be located in the outflow or in the warm, upper layers of a flared disk (France et al. 2012). In the latter case, the dominant pumping source for the fluorescent H_2 emission is the strong stellar Lyα emission.

4.1. Outflow origin of the FUV H_2 emission

To interpret the observed spatial distribution of the H_2 emission (see Fig. 3), we must investigate whether the two voids are due to absorption, or whether they are due to a lack of H_2 emission at intermediate distances to the jet axis. The H_2 emission feature close to the jet axis does not provide additional insight, because H_2 might be reformed behind an internal shock front within the outflow (Raga et al. 2005).

For a standard gas-to-dust ratio, a column density equivalent of $N_H = 7.6 \times 10^{20}$ cm^{-2} is required for $\tau_{FUV} = 1$ using the

---

[8] The shape of the PSF of this artificial image is not well known. Here, we use the width of the Gaussian fitted to a STIS image of a point source ($\sigma = 37$ mas). However, the spatial extent of the continuum along the jet direction in the G750M spectra is $\sigma = 50$ mas, and so the [S II] emission might be slightly more concentrated than shown in Fig. 3, bottom.

[9] A small fraction of the H_2 lines contributing to our FUV images might be pumped by other lines, e.g., C IV.

Fitzpatrick (1999) FUV extinction law averaged between 1400 Å and 1650 Å and $N_H = 1.8 \times 10^{21} A_V$ cm^{-2} (Predehl & Schmitt 1995). This is compatible with the attenuation of the hot, X-ray emitting plasma which is probably located close to the jet axis at distances of 30−40 AU from DG Tau ($N_H \approx 1.1 \times 10^{21}$ cm^{-2}; Güdel et al. 2007). On the other hand, this column density requires an average jet density of $n_H \gtrsim 10^6$ cm^{-3} assuming a circular jet cross-section with a diameter of $0\rlap{.}''3$ (42 AU= 6.3×10^{14} cm) at a distance of $0\rlap{.}''2$ (40 AU) from DG Tau. At this position, we estimate a density of $n_H \lesssim 2 \times 10^6$ cm^{-3} for the high-velocity jet component by extrapolating the measurement of Coffey et al. (2008) assuming a conical jet. The lower velocity jet components are located at larger distances to the jet axis and their density is lower by a factor of two. Therefore, the density required for $\tau_{FUV} = 1$ already appears to be high since a volume filling factor of about unity would be required for the estimated densities which appears unlikely for stellar jets. We note that we neglect H$_2$ line absorption, because the material along the line-of-sight differs in velocity due to the onion-like velocity structure of the jet with faster streamlines closer to the jet axis (Bacciotti et al. 2000).

This interpretation is compatible with the observed near-IR lines assuming that they originate in close spatial proximity of the FUV H$_2$ lines (which their similar shape and their approximately similar velocities suggest, see below). The absorption in the near-IR is strongly reduced compared to the FUV. For example, the transmission is three times larger for the 2.12 μm H$_2$ line than for the FUV lines assuming $E(B − V) = 0.18$, i.e., the estimated extinction of the hot, X-ray emitting plasma close to the jet axis. This ratio increases for larger column densities. Therefore, the V-shape of the near-IR H$_2$ emission also indicates a lack of intrinsic H$_2$ emission at small and intermediate distances from the jet axis.

With this interpretation, the voids in the H$_2$ emission originate from a lack of warm H$_2$ ($T \approx 2000$ K) or from a lack of pumping Lyα photons at the location of the warm H$_2$ gas. The models for molecular outflows by Panoglou et al. (2012) suggest that H$_2$ survives mainly in the outer layers of a disk wind and that the temperatures of the streamlines launched at 1 AU are in the required range (∼2000 K). Streamlines launched closer to the star have a lower H$_2$ abundance and higher temperatures which can explain the lack of (FUV) H$_2$ emission at smaller distances to the jet axis. In this scenario, the decreasing sharpness of the rim edges is a natural consequence of an optically thin cone with an increasing wall-thickness.

The wide opening-angle close to the source resembles the bubble-like features already discussed by Bacciotti et al. (2000). Comparing the FUV H$_2$ emission with the optical jet traced by [S II] λ6731 emission ($T \sim 10^4$ K, cf. Fig. 3, bottom), we find that the distance of the rim to jet axis is about twice as large as the 1-σ width of the [S II] emission. The mean velocity of the [S II] emitting material shown in Fig. 3 is −40 to −70 km s^{-1} (higher velocities pertain to the regions closer to the jet axis) which is about twice the velocity of the FUV H$_2$ lines (−10 to −30 km s^{-1}, GHRS; −9.2 ± 0.9 km s^{-1}, STIS E140M; −27 km s^{-1}, G140M; −20 . . . −30 km s^{-1}; see Ardila et al. 2002; Herczeg et al. 2006; Schneider et al. 2013, respectively). The FUV H$_2$ velocities are comparable with those of the near-IR H$_2$ lines (−20 km s^{-1}, −2 ± 18 km s^{-1}, and −9 km s^{-1}; see Takami et al. 2004; Beck et al. 2008; Greene et al. 2010, respectively). According to Ferreira et al. (2006), the poloidal velocities are inversely proportional to the launching radius for similar magnetic lever arms, which fits perfectly considering that the extent of the

H$_2$ emission perpendicular to the jet axis is about twice as large as that of the [S II] emission.

Another tracer of the molecular outflow is CO line emission (e.g., Herczeg et al. 2011) that has also been detected in the DG Tau outflow by Podio et al. (2012). In CO, V-shaped morphologies are quite common on larger scales (e.g., Arce & Sargent 2006) and can be interpreted as the interaction of a wide opening-angle outflow with the envelope (Offner et al. 2011). The expected opening-angle of such a wind is comparable to the measured opening-angle of 90° for DG Tau and we speculate that the shocks develop because of the interaction of the wide opening-angle wind with the extended atmosphere of the disk or with the innermost remnants of the envelope. This might also explain the stationary appearance of the rims.

The CO emission is unresolved in *Herschel*/PACS observations (Podio et al. 2012), but the large CO luminosity and high-excitation lines argue for excitation in C-type shocks and against an origin in the disk. In general, typical shock velocities required to excite the CO emission are a few 10 km s^{-1} while measured line-shifts are often only a few km s^{-1}. Recently Podio et al. (2013) found a blue-shifted wing of CO emission with velocities of a few km s^{-1} for DG Tau. Those CO velocities are factors of a few below the H$_2$ velocities, so that extrapolating our H$_2$ vs. [S II] λ6731 results, we expect the CO to be located outside the H$_2$ cone.

We consider an origin of the FUV H$_2$ emission in the disk atmosphere to be unlikely. First, it cannot explain the observed blue-shifted velocities, because no line shifts are expected due to (Kepler-) rotation. Second, it requires an unlikely massive outflow, because the emission from the far-side of the disk needs to be absorbed by the outflow filling the region above the disk surface. Third, it requires that the faster FUV H$_2$ emission be located at larger distances from the jet axis than the slightly slower near-IR H$_2$, because the near-IR lines are excited by shocks which are unlikely to occur deeper within the disk than the fluorescent FUV H$_2$ emission. Therefore, all observed properties of the FUV H$_2$ indicate a disk wind origin.

4.2. The pumping source

The FUV H$_2$ emission requires continuous (Lyα) pumping, because the lifetime of the upper levels is about 14 orders of magnitude shorter than that of the near-IR ro-vibrational transitions (10^{-8} vs 10^6 s). There are different possible sources for pumping Lyα photons: DG Tau itself, Lyα emission from fast shocks within the atomic jet illuminating the cone of warm H$_2$, and low-velocity shocks almost co-spatial with the H$_2$ emission. The ratios of the FUV H$_2$ lines do not change along the jet axis arguing for a similar excitation emission close to DG Tau and farther out. However, the innermost region around DG Tau is invisible so that the on-source spectrum might be different as in the case of T Tau (Walter et al. 2003; Saucedo et al. 2003). On the other hand, we would expect that, in a first order approximation, the surface luminosity drops approximately as ∼r^{-2} with distance r from DG Tau, if the stellar FUV flux is the dominant excitation source. Figure 4 shows the radial dependence of the count-rate. At larger distances, the r^{-2} model reasonably describes the data, but for $r \lesssim 0\rlap{.}''4$ the model with r^{-1} provides a better description of the data. The largest deviation from the r^{-2} model is caused by the knee corresponding to the rims and the jet-like feature ($r = 0\rlap{.}''2 . . . 0\rlap{.}''4$, a projection along the rims also shows a similar excess in the knee region). This is also present in the data analyzed by Beck et al. (2008) at the same location. It is therefore unlikely that the spatial H$_2$ luminosity distribution is caused
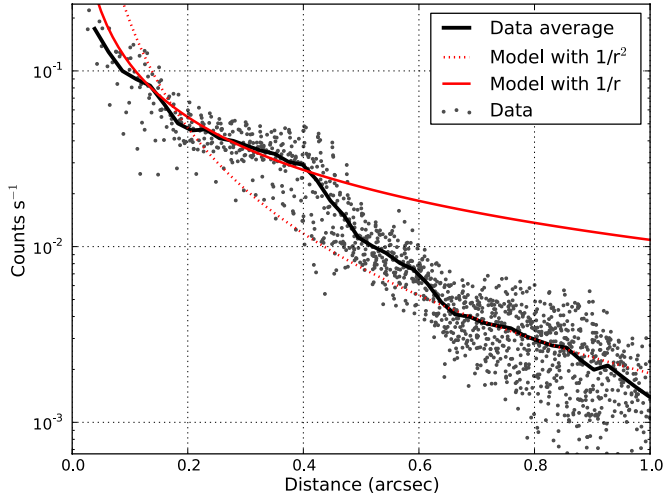
Fig. 4. Count-rate as a function of distance from the nominal DG Tau position. The data have been extracted within the 90° cone indicated in Fig. 3. The two models differ in their normalization.

Fig. 5. Inner part of the C IV emission. The circle shows the approximate region of the C IV emission seen in the STIS long-slit spectrum.

by inhomogeneties of the Lyα radiation field since the near-IR H$_2$ emission is probably shock excited (Beck et al. 2008; Takami et al. 2004) and not pumped by FUV photons. However, we note that the outflow momentum argument of Takami et al. (2004) might overestimate the momentum, because the V-shape of the emission was not known at that time. The V-shape provides a larger illuminated surface area for the UV photons and a single streamline can be excited multiple times (similar to the emission from multiple, unresolved shocks within an outflow). Therefore, less outflowing mass would be required compared to a single dense clump. Thus, we consider the measured line ratios of Beck et al. (2008) to be the strongest indication for shock excitation of the near-IR lines. In any case, we favor a scenario in which the spatial distribution of the H$_2$ emission is dominated by the amount of warm H$_2$ and not by inhomogeneities in the Lyα radiation field.

We now investigate whether the observed FUV H$_2$ emission can be pumped by the FUV flux associated with the high-velocity shocks ($v_{shock} \gtrsim 100\,\mathrm{km\,s^{-1}}$) close to the jet axis traced by C IV $\lambda\lambda$1548, 1551, and X-ray emission, or by low-velocity shocks ($v_{shock} \sim 30\,\mathrm{km\,s^{-1}}$) that are probably farther away from the jet axis. Curiel et al. (1995) found that the conversion of Lyα flux to H$_2$ fluorescence emission might be relatively efficient (about 15%). The total H$_2$ flux (see Sect. 2.2) would therefore require a Lyα luminosity in excess of $2 \times 10^{-12}\,\mathrm{erg\,s^{-1}\,cm^{-2}}$. Shock models for high velocity shocks ($v_{shock} \gtrsim 150\,\mathrm{km\,s^{-1}}$, Hartigan et al. 1987) predict Lyα luminosities $\lesssim$10 times higher than C IV luminosities. Thus, the Lyα luminosity associated with these high-velocity shocks is, based on the observed C IV luminosity, insufficient to power the H$_2$ emission by about an order of magnitude as $L_{\mathrm{C\,IV}} \approx 0.1 L_{\mathrm{H_2}}$. For lower velocity shocks, the ratio between Lyα and C IV emission increases, so that slower shocks can provide a sufficient Lyα photon flux without increasing the emission from higher temperature plasma tracers such as C IV. These lower velocity shocks would be visible in [O I] λ6300. Using the Hartigan et al. (1987) models, we estimate that the Lyα luminosity is more than about 30 times the [O I] λ6300 luminosity. Assuming that the [O I] emission is dominated by shocks with a velocity of about 30−100 km s^{-1}, only a small percentage of the Lyα photons are needed to pump the fluorescent H$_2$ emission for the detected luminosity. We therefore favor these low velocity shocks as the origin of the pumping Lyα photons.
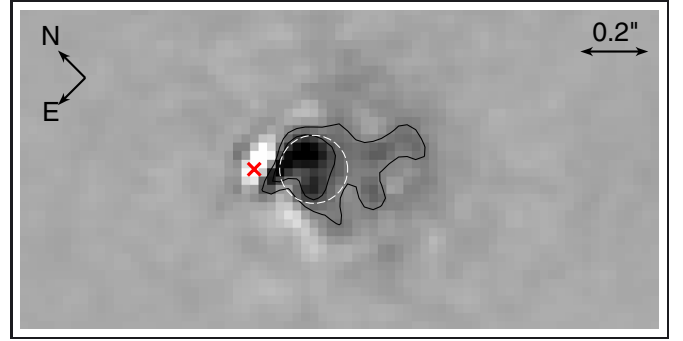
5. The intermediate temperature jet traced by C IV emission: results and discussion

Our C IV image is shown in Fig. 5. Although this image is affected by some reduction artefacts, it demonstrates that the majority of the emission falls within a circle about $0\rlap{.}''2$ from DG Tau with $r = 0\rlap{.}''1$, i.e., compatible with the region where the C IV is seen in the STIS long-slit spectrum (Schneider et al. 2013).

Schneider et al. (2013) discuss some scenarios resulting in stationary C IV emission including magnetic heating, a hot inner wind (e.g., a stellar wind) and strong shocks within the jet, possibly caused by collimation. Another interesting scenario is that instabilities within the jet lead to a number of small, unresolved shocks. In the models of Staff et al. (2010), the plasma temperature close to the jet axis is a few times 10^5 K. The heating of this high-temperature plasma is caused by numerous smaller shocks due to instabilities, e.g., kinks and wobbles within the jet. The jet is initially stabilized by magnetic fields, but beyond a certain point instabilities develop. The corresponding region is probably close to the Alfvén surface explaining that collimation is observed at similar scales. This could explain the observed offset between the peak of the hot plasma and the stellar position and that the high-temperature plasma is constantly located at the same distance from the source.

6. The outer knots: results and discussion

The outer knots are visible in all three filter images (see Fig. 1). The distances of the knots compare well with the positions observed in the optical STIS spectrum ($7\rlap{.}''2$ and $13\rlap{.}''2$)[10] indicating that the FUV emission largely overlaps with the optical jet seen in [S II] λ6731, for example. The knot at 7″ does not show a bow-like structure but appears rather circular. Nevertheless, regions of higher surface brightness tend to be located slightly closer to the shock front. The count-rates of the outer knots integrated over a circle of 2 arcsec are only about 5% of that of the inner emission component, but the region of the STIS long-slit spectrum contains less than 1% of the counts observed in a similar region close to DG Tau, which explains why they were not detected in the STIS long-slit spectrum. The integrated count ratios between the filters differ from the ratios obtained close to DG Tau so that we cannot constrain the spectral origin of the emission.

The outer FUV emission is located farther away from DG Tau than the resolved outer X-ray knot (Güdel et al. 2008;

---

[10] For a typical knot velocity in the DG Tau jet of 300 km s^{-1}, the proper-motion between the two observations is about $0\rlap{.}''1$.

Güdel et al. 2012), which has an expected position during the observations of about 6 ± 0″.5. This offset between the X-ray and FUV emission is incompatible with a scenario where the FUV *and* the X-ray emission originate from the same (forward) shock. A reverse facing shock might explain this pattern; however, we regard this to be unlikely since both the optical and X-ray knots move with rather similar velocities into the forward jet direction. On the other hand, it is possible that the X-rays trace the jet shock/Mach disk. Depending on the density contrast between the medium in front of the fast jet and that of the fast jet itself, bow shock and Mach disk have different shock velocities. If the medium in front of the jet is denser than the jet itself, the velocity of the Mach disk is higher than that of the bow shock (Hartigan 1989).

Alternatively, the X-ray emitting plasma could have been heated a few years before the X-ray observations, since its cooling time is rather long, several years according to Güdel et al. (2008). Thus, the X-ray emitting plasma might be the reminiscence of older shocks, which are not visible in lower temperature tracers any longer because of the higher radiative cooling rate at lower temperatures (an order of magnitude for $T \sim 10^5$ K at the same density).

7. Summary and conclusions

We present high spatial resolution FUV images of the DG Tau jet and construct images tracing H_2 and C IV emission. The H_2 image shows that the emission is concentrated into the forward jet direction. The H_2 emission consists of a cone with two bright rims which are slightly asymmetric. They are unresolved close to DG Tau and reach out to a radial distance of about 50 AU. Additionally, there is H_2 emission close to the jet axis. The bright rims are also seen in near-IR H_2 lines with a very similar spatial morphology (Beck et al. 2008). We conclude that the origin of the bright rims is enhanced emission close to the surface of a wide opening-angle cone and absorption of the far side of the outflow by material located close to the jet axis. The stationarity of this feature indicates that the emission is not caused by individual knots but rather is due to ongoing heating by local shocks. These low velocity shocks also provide the Lyα photons required for the FUV H_2 emission. Additional fluorescent H_2 emission excited by stellar Lyα photons might explain the excess emission seen close to DG Tau and the overall radial dependence of the H_2 emission. Extended disk-wind models by Panoglou et al. (2012) show that molecular hydrogen can survive in the outer streamlines and the H_2 emission is indeed located about twice as far from the jet axis as the faster [S II] emission. Therefore, the H_2 emission probably traces the outer part of a disk wind and the voids originate from a lack of sufficient H_2 interior of the rims.

The C IV image shows that the hot plasma is confined to the region close to the jet axis which was covered by the STIS long-slit spectrum (Schneider et al. 2013). The FUV emission seen at the position of the outer knots overlaps with low temperature plasma ($T \sim 10^4$ K) while being offset from the X-ray emission.

These results are consistent with a picture of the DG Tau jet, in which the high-velocity part of the jet is launched at small distances from DG Tau while the low-velocity part of the outflow, i.e., the molecular outflow, is less collimated with an opening angle of about 90° and is probably launched at larger distances from DG Tau. Its emission and shape is stationary over five years and unrelated to individual knots. Monitoring of the higher temperature plasma is required to check its relation to knots.

References

Agra-Amboage, V., Dougados, C., Cabrit, S., & Reunanen, J. 2011, A&A, 532, A59
Anderson, J. M., Li, Z.-Y., Krasnopolsky, R., & Blandford, R. D. 2003, ApJ, 590, L107
Arce, H. G., & Sargent, A. I. 2006, ApJ, 646, 1070
Ardila, D. R., Basri, G., Walter, F. M., Valenti, J. A., & Johns-Krull, C. M. 2002, ApJ, 566, 1100
Bacciotti, F., Mundt, R., Ray, T. P., et al. 2000, ApJ, 537, L49
Bacciotti, F., Ray, T. P., Mundt, R., Eislöffel, J., & Solf, J. 2002, ApJ, 576, 222
Beck, T. L., McGregor, P. J., Takami, M., & Pyo, T.-S. 2008, ApJ, 676, 472
Coffey, D., Bacciotti, F., Ray, T. P., Eislöffel, J., & Woitas, J. 2007, ApJ, 663, 350
Coffey, D., Bacciotti, F., & Podio, L. 2008, ApJ, 689, 1112
Curiel, S., Raymond, J. C., Wolfire, M., et al. 1995, ApJ, 453, 322
Dougados, C., Cabrit, S., Lavalley, C., & Ménard, F. 2000, A&A, 357, L61
Eislöffel, J., & Mundt, R. 1998, AJ, 115, 1554
Ferreira, J., Dougados, C., & Cabrit, S. 2006, A&A, 453, 785
Fitzpatrick, E. L. 1999, PASP, 111, 63
France, K., Schindhelm, E., Herczeg, G. J., et al. 2012, ApJ, 756, 171
Fruscione, A., McDowell, J. C., Allen, G. E., et al. 2006, in SPIE Conf. Ser., 6270
Greene, T. P., Barsony, M., & Weintraub, D. A. 2010, ApJ, 725, 1100
Güdel, M., Skinner, S. L., Briggs, K. R., et al. 2005, ApJ, 626, L53
Güdel, M., Telleschi, A., Audard, M., et al. 2007, A&A, 468, 515
Güdel, M., Skinner, S. L., Audard, M., Briggs, K. R., & Cabrit, S. 2008, A&A, 478, 797
Güdel, M., Audard, M., Bacciotti, F., et al. 2012, ASP Conf., 448, 617
Hartigan, P. 1989, ApJ, 339, 987
Hartigan, P., Raymond, J., & Hartmann, L. 1987, ApJ, 316, 323
Herczeg, G. J., Linsky, J. L., Walter, F. M., Gahm, G. F., & Johns-Krull, C. M. 2006, ApJS, 165, 256
Herczeg, G. J., Brown, J. M., van Dishoeck, E. F., & Pontoppidan, K. M. 2011, A&A, 533, A112
Hernandez, S., et al. 2012, Baltimore: STScI
Lavalley, C., Cabrit, S., Dougados, C., Ferruit, P., & Bacon, R. 1997, A&A, 327, 671
Lavalley-Fouquet, C., Cabrit, S., & Dougados, C. 2000, A&A, 356, L41
Maurri, L., Bacciotti, F., Podio, L., et al. 2013, A&A, submitted
Meliani, Z., Casse, F., & Sauty, C. 2006, A&A, 460, 1
Mundt, R., & Fried, J. W. 1983, ApJ, 274, L83
Mundt, R., Brugel, E. W., & Buehrke, T. 1987, ApJ, 319, 275
Offner, S. S. R., Lee, E. J., Goodman, A. A., & Arce, H. 2011, ApJ, 743, 91
Panoglou, D., Cabrit, S., Pineau Des Forêts, G., et al. 2012, A&A, 538, A2
Podio, L., Kamp, I., Flower, D., et al. 2012, A&A, 545, A44
Podio, L., Kamp, I., Codella, C., et al. 2013, ApJ, 766, L5
Predehl, P., & Schmitt, J. H. M. M. 1995, A&A, 293, 889
Raga, A. C., Williams, D. A., & Lim, A. J. 2005, Rev. Mex. Astron. Astrofis, 41, 137
Rodríguez, L. F., González, R. F., Raga, A. C., et al. 2012, A&A, 537, A123
Saucedo, J., Calvet, N., Hartmann, L., & Raymond, J. 2003, ApJ, 591, 275
Schindhelm, E., France, K., Burgh, E. B., et al. 2012, ApJ, 746, 97
Schneider, P. C., & Schmitt, J. H. M. M. 2008, A&A, 488, L13
Schneider, P. C., Eislöffel, J., Güdel, M., et al. 2013, A&A, 550, L1
Shang, H., Glassgold, A. E., Shu, F. H., & Lizano, S. 2002, ApJ, 564, 853
Solf, J., & Boehm, K. H. 1993, ApJ, 410, L31
Staff, J., Niebergal, B., Ouyed, R., Pudritz, R., & Cai, K. 2010, ApJ, 722, 1325
Takami, M., Chrysostomou, A., Ray, T. P., et al. 2004, A&A, 416, 213
Takami, M., Beck, T. L., Pyo, T.-S., McGregor, P., & Davis, C. 2007, ApJ, 670, L33
Testi, L., Bacciotti, F., Sargent, A. I., Ray, T. P., & Eislöffel, J. 2002, A&A, 394, L31
Walter, F. M., Herczeg, G., Brown, A., et al. 2003, AJ, 126, 3076
Wolfire, M. G., & Königl, A. 1991, ApJ, 383, 205